Available online at www.sciencedirect.com

ScienceDirect

Advances in Space Research 59 (2017) 236–251

ADVANCES IN SPACE RESEARCH (a COSPAR publication)

www.elsevier.com/locate/asr

Stereovision-based pose and inertia estimation of unknown and uncooperative space objects

Vincenzo Pesce [a,*], Michèle Lavagna [a], Riccardo Bevilacqua [b]

[a] Dipartimento di Scienze e Tecnologie Aerospaziali, Politecnico di Milano, Italy
[b] Mechanical and Aerospace Department, University of Florida, Gainesville, FL, United States

Received 4 May 2016; received in revised form 20 September 2016; accepted 1 October 2016
Available online 10 October 2016

Abstract

Autonomous close proximity operations are an arduous and attractive problem in space mission design. In particular, the estimation of pose, motion and inertia properties of an uncooperative object is a challenging task because of the lack of available a priori information. This paper develops a novel method to estimate the relative position, velocity, angular velocity, attitude and the ratios of the components of the inertia matrix of an uncooperative space object using only stereo-vision measurements. The classical Extended Kalman Filter (EKF) and an Iterated Extended Kalman Filter (IEKF) are used and compared for the estimation procedure. In addition, in order to compute the inertia properties, the ratios of the inertia components are added to the state and a pseudo-measurement equation is considered in the observation model. The relative simplicity of the proposed algorithm could be suitable for an online implementation for real applications. The developed algorithm is validated by numerical simulations in MATLAB using different initial conditions and uncertainty levels. The goal of the simulations is to verify the accuracy and robustness of the proposed estimation algorithm. The obtained results show satisfactory convergence of estimation errors for all the considered quantities. The obtained results, in several simulations, shows some improvements with respect to similar works, which deal with the same problem, present in literature. In addition, a video processing procedure is presented to reconstruct the geometrical properties of a body using cameras. This inertia reconstruction algorithm has been experimentally validated at the ADAMUS (ADvanced Autonomous MUltiple Spacecraft) Lab at the University of Florida. In the future, this different method could be integrated to the inertia ratios estimator to have a complete tool for mass properties recognition.

Keywords: Pose and inertia estimation; Stereo-vision; Autonomous close proximity operations; Resident space object; Video processing

1. Introduction

Over the past few decades, spacecraft autonomy has become a very important aspect in space mission design. In this paper, autonomous spacecraft proximity operations are discussed with particular attention to the estimation of position and orientation (pose), motion and inertia properties of an uncooperative object. The precise pose and motion estimation of an unknown object, such as a Resident Space Object (RSO) or an asteroid has many potential applications. In fact, it allows autonomous inspection, monitoring and docking. However, dealing with an uncooperative space body is a challenging problem because of the lack of available information about the motion and the structure of the target. The interest of the main space agencies, in these years, is focused on the gradual automation of the space missions because of its large number of practical applications. In this way, the high risks and costs deriving from the presence of humans on-board can be

* Corresponding author.
E-mail addresses: vincenzo.pesce@polimi.it (V. Pesce), michelle.lavagna@polimi.it (M. Lavagna), bevilr@ufl.edu (R. Bevilacqua).

http://dx.doi.org/10.1016/j.asr.2016.10.002
0273-1177/

significantly reduced. For example, in 2005, NASA sponsored the DART (Demonstration for Autonomous Rendezvous Technology) (Clohessy, 2006) project to develop and demonstrate automated navigation and rendezvous for a spacecraft. DARPA, in 2007, launched the Orbital Express mission (Friend, 2008) aimed at developing an approach for autonomous satellites servicing in orbit. Moreover, relative navigation between non-cooperative satellites can become a powerful tool in missions involving objects that cannot provide effective cooperative information, such as faulty or disabled satellite, space debris, hostile spacecraft and asteroids. In particular, the precise pose and motion estimation of an uncooperative object has possible applications in the space debris removal field. Space debris includes all man-made defunct objects, in Earth orbit or re-entering the atmosphere. The pose and the inertia matrix estimation is the first step to implement a system to recover and remove elements harmful to operational and active satellites. Additionally, the obtained algorithm can be installed on autonomous spacecraft for close-proximity operations to asteroids or for rendezvous manoeuvres. In this regard, for the near future, ESA is developing a mission for space debris removal, e.DeOrbit (Biesbroek et al., 2013) that plans to capture derelict satellites adrift in orbit. No matter what technology will be used, the estimation of the relative state will be a main technical challenge. This step will be necessary for assessing the condition of a drifting object, left in an uncertain state, and to approach it. Furthermore, the mission AIDA (Galvez et al., 2013), planned for the 2022, will be the first mission to demonstrate asteroid impact hazard mitigation by using a kinetic impactor to deflect an asteroid. To do this, an Asteroid rendezvous spacecraft is needed and it has to precisely and autonomously estimate the relative state of the asteroid, before and after the impact. Moreover, implementing autonomous robotic systems able to perform autonomous inspection, docking, on-orbit servicing and refueling, would represent a big step in the space operations field. All these operations are nowadays performed by manned systems and the main agencies are trying to automatize these processes. For this reason, this paper wants to present algorithms enabling the knowledge of the relative state, in particular, it focuses on the problem of how to estimate the relative state and the inertia matrix of an unknown, uncooperative space object using only stereoscopic measurements. This information is provided by two cameras. The methodology developed to solve this problem has many potential applications in other fields (iceberg-relative navigation (Kimball, 2011), biomedical applications (Grasa et al., 2011), vision-based unmanned aerial vehicle navigation (Bryson and Sukkarieh, 2007), etc.). Current literature addresses the problem of relative state estimation with respect to an uncooperative object, assuming partial knowledge of the geometry or feature points of the target (Philip and Ananthasayanam, 2003). In other cases, multiple spacecraft or sensors with high power consumption (3D-sensors Lichter et al., 2004, 2005 or LIDAR Shahid and Okouneva, 2007; Fenton, 2008) are utilized to compensate for the lack of information. The algorithms exploiting LIDAR have also the disadvantage of being computationally expensive. In this sense, some recent works try to reduce the computational cost of this kind of techniques (Opromolla et al., 2015b; Liu et al., 2016). None of these proposed algorithms has been physically implemented in a real application, one main reason being their high computational cost. One of the main contribution in literature, addressing relative state estimation of an uncooperative target is from Lichter (Lichter et al., 2004, 2005). He solves the problem of estimating the relative pose, motion and structure using a 3D vision sensor. This creates and processes point clouds to reconstruct the geometric shape of the object. From this information, he is able to extract a rough measurement of the centroid and rotation matrix. Then, two Kalman Filters (translation and rotation) are used to estimate the state and inertia properties. However, using 3D sensor involves more power consumption, computational cost and data to manage. In 2013, Segal and Gurfil presented a solution of the state estimation of a non-cooperative spacecraft using an Iterated Extended Kalman Filter (IEKF) (Segal et al., 2011, 2014). Their approach was the baseline for this research. They develop and utilize a translational-rotational coupled model to describe the relative dynamics. Then, an IEKF is used to estimate the state. The basic assumption is to have only stereoscopic measurements. However, they do not estimate the inertia matrix, but they run N Kalman filters in parallel and, at the end, they choose the best value for the inertia tensor according to a Maximum A Posteriori (MAP) estimation. Thus, N filters must work simultaneously for an interval of time t to estimate the state. Then, all the estimated states are compared and the selected inertia matrix is the one that provides better results in terms of state error. This method clearly cannot be implemented on a real spacecraft because of the large computational cost needed in problems without previous knowledge of geometry information. Another method for the estimation of the inertia matrix was proposed in Benninghoff and Boge (2015). They solve a constrained least squares problem for the estimation of the center of mass and inertia properties. However, they do not model the observations, assuming to know all the dynamical quantities with noise. For this reason, the analyzed scenario is not very realistic. A very interesting work was published by Tweddle and Saenz-Otero (2014) and Tweddle (2013). Assuming a stationary leader, he developed a method to estimate the state and structure of an unknown object using a smoothing algorithm. Smoothing and Mapping (SAM) are commonly used for simultaneous localization and mapping (SLAM) problems. This method estimates the complete 'robot' trajectory in time and not only the current pose. The particular smoothing algorithm used by Tweddle is the Incremental Smoothing Algorithm (iSAM) introduced by Kaess et al. (2008, 2007). This method performs fast incremental updates to compute a

full map and trajectory of the object at any time. However, this method does not handle properly trajectory with loops, non-linear problems and it is used only for offline implementations. In our work, a Kalman Filter has been selected as estimator for its good computational performance. In fact, Strasdat et al. (2010) clearly expresses how the smoothing algorithm is more accurate but also less computationally efficient than the classical filters. Moreover, differently from smoothing algorithms, filtering techniques can successfully deal with problems involving high uncertainties. The assumption of an uncooperative target has been carried out to have the possibility to apply the obtained results to a wide number of applications. Uncooperative objects have no target identifiers (such as optical feature points) and proximity sensors. This makes the estimation more difficult and less accurate, but more applicable to a vast range of in-space objects. With this assumption, it is possible to expand the applicability of this work to asteroids and completely unknown objects. Recent works by Dong and Zhu (2016a,b) assess the problem of relative pose estimation of an uncooperative object. However, they use a simple equation for the propagation of the state that does not involve any inertia information.

Another aspect to take into account, when dealing with filtering procedure, is that the initial condition of the relative state has to be accurate enough. Several works are present in literature that address and try to solve this kind of problem. In particular, in DAmico et al. (2014), the problem of estimating the pose of a passive resident space object, without any a-priori knowledge of its state, is solved. They use a mono camera setup and exploit computer vision techniques. However, they also assume to have information about the 3D geometrical model of the object. This is common in this kind of algorithms but it is not an unrealistic assumption. In fact, some previous partial information about resident space objects can be available in many real cases. A similar approach was proposed by Opromolla et al. (2015a) in which, instead, they exploit a LIDAR. In particular, they process the point cloud obtained with the sensor, to initialize a template matching technique. Even in this case, some information about the 3D model of the object is necessary. Finally, it is worth to report (Sharma et al., 2016) that offers a global overview of the techniques used for initial pose estimation.

Since the inertia properties of a body influence the contact and impact dynamics, it is a crucial aspect to perform docking with the inspected object. In Felicetti et al. (2014) the inertia matrix of the chaser-target system is estimated but only after an initial docking. This is possible by applying a sequence of small pulses. However, the estimation of the inertia matrix, in torque-free motion conditions, is a very difficult task and one of the open points that this work tries to solve. Using a pseudo-measurement equation in the observation model with an appropriate parametrization, the ratios of the components of the inertia matrix can be recovered. The intended advancements in the state of the art for relative state and inertia estimation are:

- Improve the relative state estimation with respect to the works present in the actual literature.
- Estimate the ratios of the inertia matrix components for a correct relative dynamics propagation, exploiting a novel approach.
- Reconstruct the complete inertia matrix with an offline image processing method.

The paper is organized as follows. Section 2 presents the description of the used dynamical model. In Section 3 the observation model is analyzed. In Section 4 the formulation for the inertia ratios estimation is presented in a detailed way. Section 5 describes the filtering procedures used for the estimation. Section 6 is dedicated to the discussion of the main results. These results are obtained through several numerical simulations. Section 7 presents the details of the inertia reconstruction procedure via image processing. In Section 8 the conclusions and possible future developments are drawn.

2. Dynamical model

Correct modeling of relative translational and rotational motion is essential for autonomous missions. In literature, a large number of studies about point-mass models for relative spacecraft translational motion can be found. The most famous and used model is the one presented by Clohessy and Wiltshire (Clohessy, 1960). The approximated linear equations allow a simpler representation of the dynamical model, however introducing some limitations. In particular, this model is valid for only circular target orbits and small relative distance between the two spacecraft. A different non-linearized model is here used to overcome the intrinsic constraints of the Clohessy-Wiltshire approach.

2.1. Reference frames and coordinate systems

The location of a point in a three dimensional space must be specified with respect to a reference system. Two objects are considered: a leader L and a target T. In this paper, the *leader* is the inspecting spacecraft and the *target* is the unknown, uncooperative object. The standard Earth-centered, inertial, Cartesian right-hand reference frame is used. It is defined by the center of the Earth, the Celestial North Pole and the point identifying the Vernal Equinox. The corresponding coordinate system is indicated with the letter $\mathcal{I}$ and has its origin at the Earth's center. The fundamental plane is the equator, and the positive X axis points in the vernal equinox direction. The Z axis points in the direction of the North Pole. $\mathcal{L}$ is the local-vertical, local-horizontal Euler-Hill (LVLH) coordinate system. It is fixed to the leader spacecraft's center of mass, the X unit vector directed radially outward along the direction from the center of the Earth to the spacecraft, Z normal to the leader orbital plane, and Y according to the right-hand rule. Finally $\mathcal{T}$, a Cartesian right-hand body-fixed coordi-

nate system centered on the target spacecraft's center of mass. It is also assumed that this frame is coincident with the principal axis of inertia. In this work, the frame $\mathcal{L}$ is assumed to be coincident with the Cartesian right-hand body-fixed coordinate system attached to the leader spacecraft's center of mass. The used notation is now presented. The vector $\boldsymbol{\rho}_0$ is the vector connecting the leader center of mass with the target center of mass, expressed in the leader frame. Analogously, $\boldsymbol{\rho}_i$ can be defined as the position vector, in the leader frame, between the leader center of mass and the feature point $\mathbf{P}_i$. In this paper, no previous knowledge of any feature point is assumed. Consequently, $\dot{\boldsymbol{\rho}}_0$ and $\dot{\boldsymbol{\rho}}_i$ are the translational velocities of the target center of mass and of a generic feature point, expressed in $\mathcal{L}$. The relative angular velocity is expressed as $\boldsymbol{\omega}$. This vector is the difference of the angular velocities of the leader and target respectively, expressed in the leader frame:

$$\boldsymbol{\omega} = \boldsymbol{\omega}_T|_{\mathcal{L}} - \boldsymbol{\omega}_L|_{\mathcal{L}} \tag{1}$$

The relative attitude is described using the rotation quaternion $\mathbf{q} = [q_0, q_1, q_2, q_3]^T$ where the first component is the scalar part and the other three are the vector one.

2.2. Process model

Once the fundamental parameters are defined, the problem is formulated, starting from the dynamical or process model. The classical formulation for the dynamical model in a Kalman Filter dealing with non-linear equations is:

$$\dot{\mathbf{x}} = f(\mathbf{x}) + \mathbf{w}(t) \tag{2}$$

where $\mathbf{x}$ is the state vector, $f(\mathbf{x})$ is a non-linear function describing the process and $\mathbf{w}$ is a random zero-mean white noise. In our case, the state vector is defined as:

$$\mathbf{x} = [\boldsymbol{\rho}^T, \dot{\boldsymbol{\rho}}^T, \boldsymbol{\omega}^T, \mathbf{q}^T, \mathbf{P}_i^T]^T \tag{3}$$

This is a $13 + 3N$ elements vector where N is the number of feature points. At this point the dynamical model can be described. The model derived in Gurfil and Kholshevnikov (2006) is here presented. Considering rigid bodies, the relative dynamics is described using a set of non-linear differential equations. The translational and rotational behavior are decoupled. According to Newton's Second Law, under the assumptions of no external or internal forces except gravity, spherical bodies, no tidal forces, attractor's mass much larger than the orbiting body's mass, the equations of motion of the Keplerian two-body problem can be written as:

$$\ddot{\mathbf{r}} + \mu\frac{\mathbf{r}}{r^3} = 0 \tag{4}$$

where $\mathbf{r} = [x, y, z]^T$ is the position vector in the $\mathcal{I}$ frame, μ is the Earth's gravitational constant and $r = \|\mathbf{r}\|$. This equation of motion can be written for both leader and target, replacing $\mathbf{r}$ with $\mathbf{r}_L$ and $\mathbf{r}_T$, the positions of the leader and the target in the $\mathcal{I}$ frame.

$$\ddot{\mathbf{r}}_L + \mu\frac{\mathbf{r}_L}{r_L^3} = 0 \tag{5}$$

$$\ddot{\mathbf{r}}_T + \mu\frac{\mathbf{r}_T}{r_T^3} = 0 \tag{6}$$

the relative position vector between the leader and the target can be defined as $\boldsymbol{\rho}|_{\mathcal{I}} = \mathbf{r}_T - \mathbf{r}_L$ (see Fig. 1). Subtracting Eq. (5) from Eq. (6) yields:

$$\ddot{\boldsymbol{\rho}}|_{\mathcal{I}} = \frac{\mu(\mathbf{r}_L + \boldsymbol{\rho})}{\|\mathbf{r}_L + \boldsymbol{\rho}\|^3} + \mu\frac{\mathbf{r}_L}{r_L^3} \tag{7}$$

The relative acceleration can also be expressed as:

$$\ddot{\boldsymbol{\rho}}|_{\mathcal{I}} = \frac{d^2\boldsymbol{\rho}}{dt^2} + 2\boldsymbol{\omega}_L|_{\mathcal{I}} \times \frac{d\boldsymbol{\rho}}{dt} + \frac{d\boldsymbol{\omega}_L|_{\mathcal{I}}}{dt} \times \boldsymbol{\rho} + \boldsymbol{\omega}_L|_{\mathcal{I}} \times (\boldsymbol{\omega}_L|_{\mathcal{I}} \times \boldsymbol{\rho}) \tag{8}$$

Being, by assumption, $\boldsymbol{\omega}_L|_{\mathcal{I}}$, the angular velocity of frame $\mathcal{L}$ with respect to $\mathcal{I}$, normal to the orbital plane, leads to

$$\boldsymbol{\omega}_L|_{\mathcal{I}} = [0, 0, \dot{\vartheta}_L]^T \tag{9}$$

Knowing that

$$\boldsymbol{\rho} = [x, y, z]^T \tag{10}$$

substituting Eqs. (7), (9), (10) into Eq. (8) the following equations are obtained:

$$\ddot{x} - 2\dot{\vartheta}_L\dot{y} - \ddot{\vartheta}_L y - \dot{\vartheta}_L^2 x = \frac{\mu(r_L + x)}{[(r_L + x)^2 + y^2 + z^2]^{\frac{3}{2}}} + \frac{\mu}{r_L^2} \tag{11}$$

$$\ddot{y} + 2\dot{\vartheta}_L\dot{x} + \ddot{\vartheta}_L x - \dot{\vartheta}_L^2 y = -\frac{\mu y}{[(r_L + x)^2 + y^2 + z^2]^{\frac{3}{2}}} \tag{12}$$

$$\ddot{z} = -\frac{\mu z}{[(r_L + x)^2 + y^2 + z^2]^{\frac{3}{2}}} \tag{13}$$

$\dot{\vartheta}_L$ and $\ddot{\vartheta}_L$ are the orbital angular velocity and acceleration of the leader and are equal to

$$\dot{\vartheta}_L = \sqrt{\frac{\mu}{a_L^3(1 - e_L^2)^3}}(1 + e_L\cos\vartheta_L)^2 \tag{14}$$

$$\ddot{\vartheta}_L = \frac{-2\dot{r}_L\dot{\vartheta}_L}{r_L} \tag{15}$$

This set of non-linear ordinary differential equations describes the relative translational dynamics between two objects in space, orbiting around a planet under the Newton's Law assumptions. Analogously, a model that describes the rotational motion of the target relative to the leader is illustrated. To parametrize the relative attitude, it has been decided to use a rotation matrix D which performs the transformation from the body fixed frame $\mathcal{T}$, relative to the target, to the body fixed frame $\mathcal{L}$, relative to the leader. The components of this matrix are combinations of relative quaternions q_0, q_1, q_2, q_3. Knowing the rotation matrix D, the relative angular velocity in both target and leader frames can be calculated.

$$\boldsymbol{\omega}|_{\mathcal{L}} = D\boldsymbol{\omega}_T|_{\mathcal{T}} - \boldsymbol{\omega}_L|_{\mathcal{L}} \tag{16}$$

Combining the Euler equations for both leader and target, the relative rotational dynamics can be expressed as (Segal and Gurfil, 2009):

$$\mathbf{I}_L \frac{d\boldsymbol{\omega}}{dt}|_{\mathcal{L}}^{\mathcal{L}} = \mathbf{I}_L D\mathbf{I}_T^{-1}[\mathbf{N}_T - \boldsymbol{\omega}_T|_T \times \mathbf{I}_T\boldsymbol{\omega}_T|_T] - \mathbf{I}_L\boldsymbol{\omega}_L|_{\mathcal{L}} \times \boldsymbol{\omega}_L|_{\mathcal{L}} - [\mathbf{N}_L - \boldsymbol{\omega}_L|_{\mathcal{L}} \times \mathbf{I}_L\boldsymbol{\omega}_L|_{\mathcal{L}}] \quad (17)$$

where $\mathbf{N}_T$ and $\mathbf{N}_L$ are the external torques on the target and leader. Only in the previous expressions, the symbol $a|_N$ indicates that the quantity 'a' is evaluated in the N frame, on the other hand, $(\frac{db}{dt})|^M$ indicates the derivative of the quantity 'b' in the M frame. The relative attitude kinematics is given by:

$$\dot{\mathbf{q}} = \frac{1}{2}\mathcal{Q}\boldsymbol{\omega} \quad (18)$$

with

$$\mathcal{Q}(\mathbf{q}) = \begin{bmatrix} -q_1 & -q_2 & -q_3 \\ q_0 & -q_3 & q_2 \\ q_3 & q_0 & -q_1 \\ -q_2 & q_1 & q_0 \end{bmatrix}$$

The motion of the feature points can be defined in different ways. In particular, if the motion is expressed in the leader frame:

$$\dot{\mathbf{P}}_T^i|_{\mathcal{L}} = D\dot{\mathbf{P}}_T^i|_T + \boldsymbol{\omega} \times \mathbf{P}_T^i|_{\mathcal{L}} = \boldsymbol{\omega} \times \mathbf{P}_T^i|_{\mathcal{L}} \quad (19)$$

However, the dynamics of the feature points is simpler if expressed in the target frame. In fact, due to the rigid body assumption, a feature point cannot change its relative position with respect to the target center of mass. This leads to:

$$\dot{\mathbf{P}}_T^i|_T = 0 \quad (20)$$

Considering that the center of mass dynamics is described by Eqs. (11)–(13), the position of a single feature point can be described as follows:

$$\boldsymbol{\rho}_i = \boldsymbol{\rho}_0 + \mathbf{P}_T^i|_{\mathcal{L}} \quad (21)$$

In this way, the motion of a feature point is given by the superposition of the rotational and translational dynamics. Using this formulation, for each time step, it is only necessary to integrate the position of the center of mass and add the contribution due to the rotation of the feature points. This aspect is very important from the computational point of view, for the sake of an online implementation. An important assumption inherently made herein is that the orbit of the leader is completely known. In a real application, the goodness of the leader orbit estimation will influence the accuracy of the relative motion.

3. Observation model

The purpose of this section is to describe the observation model that allows to obtain information from the collected stereoscopic images. Suppose to have two cameras in a stereo configuration mounted on the leader spacecraft $\mathcal{L}$

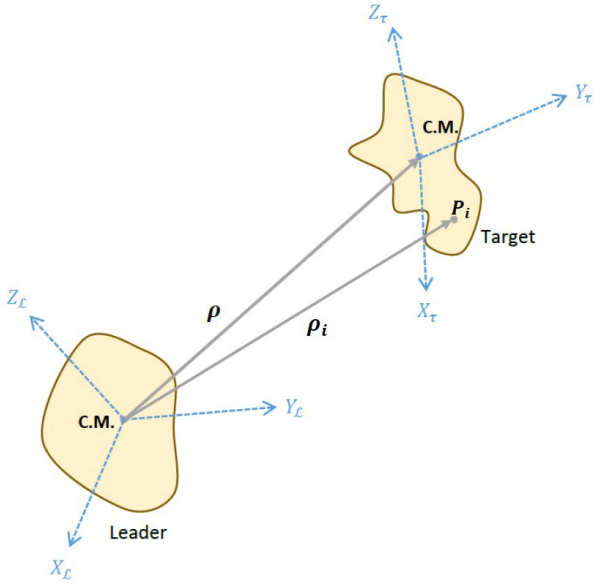

Fig. 1. Leader – target coordinate system.

as in Fig. 2. The center of projection of the right camera is assumed to coincide with the center of mass of the leader. This is also the origin of the Cartesian right-hand camera coordinate system $[X, Y, Z]$ as defined in Section 2.1. The left camera is separated by a baseline b from the right camera. Using a pinhole camera model and exploiting the perspective projection model, a point in a 3D frame is described in the 2D image plane. With this method all the selected and tracked feature points are expressed in the 2D camera plane. For the vector $\boldsymbol{\rho}_i$ connecting the leader center of mass and a generic feature point, assuming to have a focal length f equal to 1, the following expressions are derived: For the right camera

$$u_R(i) = f\frac{x_i}{y_i} \quad v_R(i) = f\frac{z_i}{y_i} \quad (22)$$

and for the left camera

$$u_L(i) = f\frac{x_i - b}{y_i} \quad v_L(i) = f\frac{z_i}{y_i} \quad (23)$$

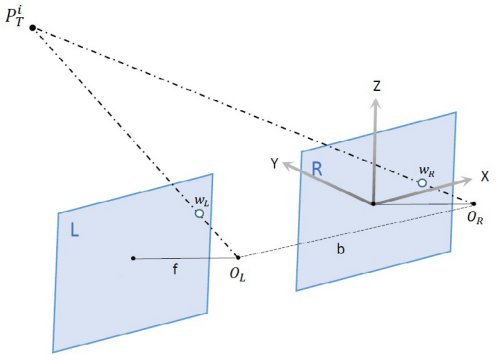

Fig. 2. Camera configuration.

where $\boldsymbol{\rho}_i = [x_i, y_i, z_i]$ is expressed in the camera frame. Eqs. (22) and (23) represent the 2D projections of a generic 3D point expressed by $[x_i, y_i, z_i]$. We can also define $\mathbf{w}_R = [u_R \; v_R]$ and $\mathbf{w}_L = [u_L \; v_L]$. Further information can be recovered from the acquired images, exploiting the optical flow. A formulation of the relation between the 3D motion and the optical flow is derived in Heeger and Jepson (1992). This relationship is expressed by the following equations:

$$\dot{\mathbf{w}}_{Ri} = \begin{bmatrix} \frac{1}{y_i} A(w_{Ri}) & B(w_{Ri}) \end{bmatrix} \begin{bmatrix} \dot{\boldsymbol{\rho}}_0 \\ \boldsymbol{\omega} \end{bmatrix} \tag{24}$$

and

$$\dot{\mathbf{w}}_{Li} = \begin{bmatrix} \frac{1}{y_i} A(w_{Li}) & B(w_{Li}) \end{bmatrix} \begin{bmatrix} \dot{\boldsymbol{\rho}}_0 \\ \boldsymbol{\omega} \end{bmatrix} \tag{25}$$

with

$$A = \begin{bmatrix} 1 & 0 & w_1 \\ 0 & 1 & w_2 \end{bmatrix} \tag{26}$$

and

$$B = \begin{bmatrix} -w_1 w_2 & 1 + w_1^2 & -w_2 \\ -1 - w_2^2 & w_1 w_2 & w_1 \end{bmatrix} \tag{27}$$

where w_1 and w_2 are the first and the second component of the vector $\mathbf{w}_R$ or $\mathbf{w}_L$. It is important to underline that, in reality, cameras collect images at a given sampling frequency. Using two subsequent frames, the optical flow can be estimated and the image velocity computed. However, in the here discussed observation model, it is assumed that the information about the image velocity is recovered at each time step exploiting only information about relative linear and angular velocity at that instant of time. Dealing with real images a proper algorithm, computing the optical flow, has to be used. Another problem is to determine the different location of the same point in the left and right image plane respectively. The resulting difference is called disparity and it is defined as:

$$d_i = u_L - u_R \tag{28}$$

The disparity allows to reconstruct information about the depth. The human brain does something similar, interpreting the difference in retinal position (Qian, 1997). In stereo vision applications, this can be performed exploiting the so called *triangulation*. A set of feature points is chosen and they are assumed to be always in the view of the cameras. Therefore, according to our assumptions, the initial set of points is always traceable. At each time step, the discrete measurement vector provided by the cameras is:

$$\mathbf{Z}_i = [\mathbf{w}_{Ri}, \mathbf{w}_{Li}, \dot{\mathbf{w}}_{Ri}, \dot{\mathbf{w}}_{Li}, d_i] \tag{29}$$

Therefore, the observation equation is:

$$\mathbf{Z}_i = h(\mathbf{x}) + \mathbf{v}(t) \tag{30}$$

with $\mathbf{v}$ random zero-mean white noise and $h(\mathbf{x})$, the observation model, given by:

$$h(\mathbf{x}) = \begin{pmatrix} \frac{x_i}{y_i} \\ \frac{z_i}{y_i} \\ \frac{x_i - b}{y_i} \\ \frac{z_i}{y_i} \\ \frac{x_i - b}{y_i} - \frac{z_i}{y_i} \\ \begin{bmatrix} \frac{1}{y_i} A(w_{Ri}) & B(w_{Ri}) \end{bmatrix} \begin{bmatrix} \dot{\boldsymbol{\rho}}_0 \\ \boldsymbol{\omega} \end{bmatrix} \\ \begin{bmatrix} \frac{1}{y_i} A(w_{Li}) & B(w_{Li}) \end{bmatrix} \begin{bmatrix} \dot{\boldsymbol{\rho}}_0 \\ \boldsymbol{\omega} \end{bmatrix} \end{pmatrix} \tag{31}$$

4. Inertia ratios estimation

For the presented model, an a priori knowledge of the target inertia matrix is necessary. This is not a realistic assumption since we are dealing with a completely unknown and uncooperative space object. To overcome this contradiction, an estimation of the basic inertia properties is necessary. A torque free motion is assumed. In this condition, the inertia matrix is not fully observable. In fact, only two of three degrees of freedom are observable (Tweddle, 2013). Thus, two parameters are sufficient to represent the inertia matrix. With a parametrized inertia matrix, the motion can be propagated in the correct way. In fact, in torque free motion, Eq. (17) can be properly propagated using the components of the inertia matrix scaled with any scale factor. However, no geometrical or mass properties can be recovered. A proper parametrization of the inertia matrix is necessary. Tweddle, in his work (Tweddle, 2013), proposed a smart inertia parametrization. In particular:

$$k_1 = ln\left(\frac{I_x}{I_y}\right) \quad k_2 = ln\left(\frac{I_y}{I_z}\right) \tag{32}$$

We decided to exploit Tweedle's idea, but including this parametrization in a filtering procedure that is more computationally efficient with respect to a smoothing algorithm. This formulation relies on the minimum number of parameters, equal to the number of degrees of freedom. k_1 and k_2 do not have any additional constraints. The inertia ratios have to be greater than zero and they can be each value up to infinity. This is a consistent parametrization because the natural logarithm has the same validity domain. Using this parametrization, the target inertia matrix can be normalized as:

$$\mathbf{I}_T = \begin{bmatrix} \frac{I_x}{I_y} & 0 & 0 \\ 0 & 1 & 0 \\ 0 & 0 & \frac{I_z}{I_y} \end{bmatrix} = \begin{bmatrix} e^{k_1} & 0 & 0 \\ 0 & 1 & 0 \\ 0 & 0 & e^{-k_2} \end{bmatrix} \tag{33}$$

At this point, these two parameters must be estimated by the filter. Therefore, a new augmented state can be defined as:

$$\mathbf{x} = [\boldsymbol{\rho}^T, \dot{\boldsymbol{\rho}}^T, \boldsymbol{\omega}^T, \mathbf{q}^T, \mathbf{P}_i^T, k_1, k_2]^T \tag{34}$$

Also the dynamical model is different. In fact, the parametrized inertia matrix will substitute the previous value of the target inertia matrix in the rotational dynamics expression. Additionally, two equations for k_1 and k_2 are considered.

$$\frac{\partial k_1}{\partial t} = 0 \tag{35}$$

$$\frac{\partial k_2}{\partial t} = 0 \tag{36}$$

Eqs. (35) and (36) are valid under the assumption of rigid body motion and without considering any mass variation. In order to improve the convergence of the filter a pseudo measurement constraint can be added. This is inserted in the observation considering a null output. In this way, no additional measurements are formally considered. With this equality constraint, the value of the inertia matrix can be forced to converge to the correct value. In particular:

$$\mathbf{0} = \dot{\boldsymbol{\omega}}_T + \mathbf{I}_T^{-1}(\boldsymbol{\omega}_T \times \mathbf{I}_T\boldsymbol{\omega}_T) \tag{37}$$

This is the new pseudo measurement. It is the classical Euler equation for the rotational dynamics of the target. As already said, this equation does not add any physical measurement and has to be inserted to the already present observation equations (31). In particular:

$$h(\mathbf{x}) = \begin{pmatrix} \frac{x_i}{y_i} \\ \frac{z_i}{y_i} \\ \frac{x_i - b}{y_i} \\ \frac{z_i}{y_i} \\ \frac{x_i - b}{y_i} - \frac{z_i}{y_i} \\ \begin{bmatrix} \frac{1}{y_i} A(w_{Ri}) & B(w_{Ri}) \end{bmatrix} \begin{bmatrix} \dot{\boldsymbol{\rho}}_0 \\ \boldsymbol{\omega} \end{bmatrix} \\ \begin{bmatrix} \frac{1}{y_i} A(w_{Li}) & B(w_{Li}) \end{bmatrix} \begin{bmatrix} \dot{\boldsymbol{\rho}}_0 \\ \boldsymbol{\omega} \end{bmatrix} \\ \dot{\boldsymbol{\omega}}_T + \mathbf{I}_T^{-1}(\boldsymbol{\omega}_T \times \mathbf{I}_T\boldsymbol{\omega}_T) \end{pmatrix} \tag{38}$$

A fundamental aspect to take into account is that in the pseudo measurement equation, the target angular acceleration is present. Information about this quantity has to be recovered from the actual measurement. However, with knowledge of $\boldsymbol{\omega}_L, \dot{\boldsymbol{\omega}}_L$ and $\boldsymbol{\omega}$, there is not an analytical expression independent on $\mathbf{I}_T$ to compute $\dot{\boldsymbol{\omega}}_T$. This implies that the angular acceleration of the target has to be measured. With the knowledge of the optical flow, the value of $\boldsymbol{\omega}$ at each time step can be recovered. Then, a numerical differentiation can be performed to find the relative angular acceleration. Dealing with derivative of a quantity affected by errors is common in many scientific fields. For this reason, several methods to compute numerical derivative of noisy data exist. In our work, since no real measurements are available, the value of $\dot{\boldsymbol{\omega}}$ is obtained by adding noise to the quantity available from the real dynamical model. The noise is modeled as a zero-mean Gaussian with standard deviation of 10^{-4} rad/s^2. This value can be obtained selecting the proper numerical differentiation algorithm as presented in Listmann et al. (2013).

5. Filtering procedure

5.1. Extended Kalman Filter

The Kalman Filter was firstly developed by Rudolf E. Kalman in 1960s (Kalman, 1960). Kalman proposed a recursive solution to the discrete-data linear filtering problem. This set of mathematical equations provides a solution to this kind of problem in a very computationally efficient way. This is one of the reasons why it was used several times in real applications, such as the Apollo navigation computer (McGee and Schmidt, 1985). One of the most widely used approaches is the Extended Kalman Filter (EKF). This procedure was introduced by Maybeck (1982) in the early 1980s. The EKF is a way to overcome the problems arising from the approximation of the system dynamics with a linear model. The general idea is to use a non-linear description of the system model and linearize this model about the state estimation for each time step. In this way, as soon as a new estimate is predicted, a linearized, more accurate state trajectory is available in the estimation process. Remembering that the linearization process involves the assumption of small deviations from the reference trajectory, this can be ensured by incorporating this updating of the reference trajectory in the estimation process. Let's assume that our process is governed by a non-linear stochastic differential equation. This equation can be expressed in non-linear state-space as:

$$\dot{\mathbf{x}} = f(\mathbf{x}) + \mathbf{w} \tag{39}$$

where $\mathbf{x}$ is the state vector, $f(\mathbf{x})$ is a non-linear function describing the model, depending on the state and $\mathbf{w}$ is a random zero-mean white noise. The related power spectral density matrix is given by:

$$\mathbf{Q} = E[\mathbf{w}\mathbf{w}^T] \tag{40}$$

In the same way, a measurement equation can be defined as a non-linear function as:

$$\mathbf{z} = h(\mathbf{x}) + \mathbf{v} \tag{41}$$

and

$$\mathbf{R} = E[\mathbf{v}\mathbf{v}^T] \tag{42}$$

with $\mathbf{v}$ being the measurement noise. The non-linear function $h(\mathbf{x})$ relates the state $\mathbf{x}$ to the measurement $\mathbf{z}$. As already said, the system and the measurement equations are non-linear. This implies that a first-order approximation has to be used in the continuous Riccati equations for the systems dynamics matrix $\boldsymbol{F}$ and the measurement matrix $\boldsymbol{H}$ respectively. These two matrices are the Jacobian of partial derivatives of f and h with respect to $\mathbf{x}$:

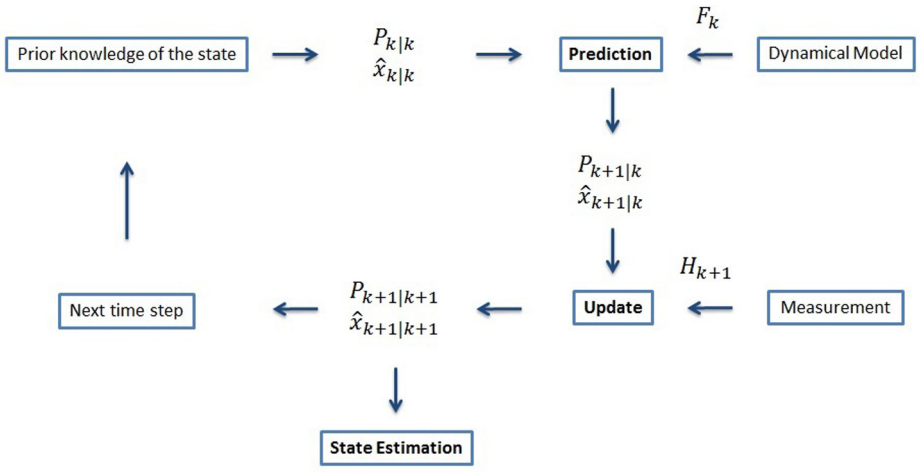

Fig. 3. Extended Kalman Filter flowchart.

$$\boldsymbol{F} = \frac{\partial f(\mathbf{x})}{\partial \mathbf{x}}|_{x=\hat{x}} \tag{43}$$

$$\boldsymbol{H} = \frac{\partial h(\mathbf{x})}{\partial \mathbf{x}}|_{x=\hat{x}} \tag{44}$$

The fundamental matrix for the discrete Riccati equations is approximated by the Taylor-series expansion for $e^{\boldsymbol{F}\Delta t}$ and can be expressed as:

$$\boldsymbol{\Phi}_k = \boldsymbol{I} + \boldsymbol{F}\Delta t + \frac{\boldsymbol{F}^2\Delta t^2}{2!} + \frac{\boldsymbol{F}^3\Delta t^3}{3!} + \ldots \tag{45}$$

where Δt is the sampling time. In general, the Taylor-series expansion is approximated with only the first two terms:

$$\boldsymbol{\Phi}_k = \boldsymbol{I} + \boldsymbol{F}\Delta t \tag{46}$$

In Fig. 3, a scheme of the filtering procedure is presented.

5.2. Iterated Extended Kalman Filter

The presented Extended Kalman Filter, is a widely used, powerful estimation method. As already said, it is used in applications with a behavior described by non-linear models. However, there are some real cases in which also the measurement equation can be highly non-linear. In the Maybeck work (Maybeck, 1982), there is also a reference to an *Iterated Extended Kalman Filter* (IEKF). With this method, for each time step, local iterations and re-linearization are performed on the updated reference state. In this way, at a fixed time k, the new state update is computed and it is used as a better state estimate for evaluating h and computing the Jacobian $\mathbf{H}$. Also in this case, a simple scheme is presented in Fig. 4. The described algorithm outperforms the simple EKF re-computing, iteratively, h and $\boldsymbol{H}$ to obtain a better state estimate $\hat{\mathbf{x}}(k+1|k+1)$. This, of course, leads to have better estimation also in the future steps. Despite the iterative cycle, the filter maintains its simplicity and computational efficiency.

6. Numerical simulations

In this section, an evaluation of the performance and robustness of the filter is performed through a Monte-Carlo analysis. A satellite and an object in low Earth orbit are considered. In particular, the leader orbit is known. It is assumed that the orbit of the leader has eccentricity $e_L = 0.05$, semi-major axis $a_L = 7170$ km, inclination $i_L = 15$ deg, argument of the perigee $\omega = 340$ deg and right ascension of ascending node $\Omega = 0$ deg. According to our parametrization, the leader inertia is

$$I_L = \begin{bmatrix} 0.83 & 0 & 0 \\ 0 & 1 & 0 \\ 0 & 0 & 1.083 \end{bmatrix} \text{kg m}^2 \tag{47}$$

In addition, two parallel cameras, in a stereo configuration and pointing in the same direction are mounted on the leader spacecraft. The baseline between the cameras is assumed equal to 1 m. These conditions are chosen similarly to the Segal's work (Segal et al., 2014), in order to have a possible comparison. Moreover, only five feature points are supposed to be measured instead of the ten chosen by Segal. This is an extreme case, in fact, more than five points are usually visible and detectable. However, this condition may occur when the object is not properly illuminated or if it is too bright. Additionally, considering only a small number of points, the robustness and convergence of the filter are tested also with poor available measurements. The detected features are assumed to be spread over the body according to a uniform distribution bounded between 1.5 m and −1.5 m. The adopted distribution of the feature points is not a rigorous choice for representing real cases. However, being the target scenario completely undefined, the most general distribution, useful for sampling arbitrary distributions, has been used. After defining the initial condition for the leader orbit, the state vector has to be initialized. The initial state vector is:

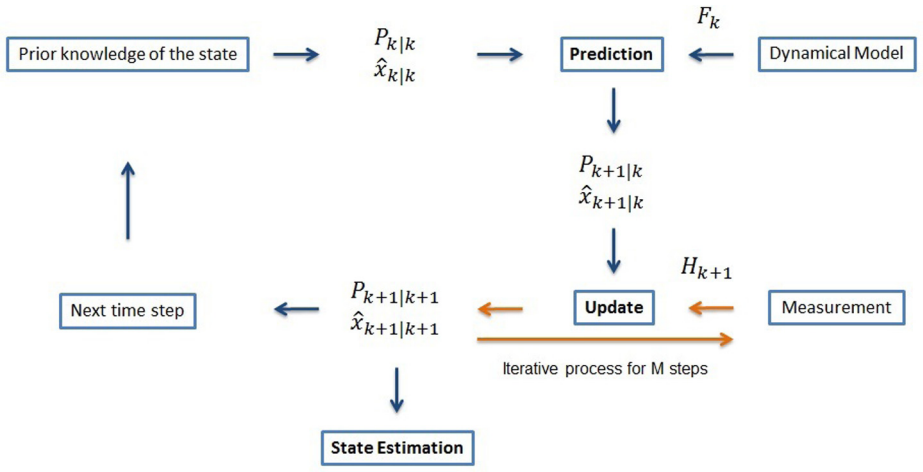

Fig. 4. Iterated Extended Kalman Filter flowchart.

$$\mathbf{x}_0 = [\boldsymbol{\rho}_0, \dot{\boldsymbol{\rho}}_0, \boldsymbol{\omega}, \mathbf{q}_0, \mathbf{P}_T^i, k_1, k_2] \tag{48}$$

This vector will be defined for each simulation. At this point, the filter parameters have to be selected. In particular, the covariance matrices **Q**, **R**, **P** have to be chosen. **R** represents the measurement noise and it can be determined whenever the sensor accuracy is given. In the following simulations, the noise of the measurements are modeled as a zero-mean Gaussian with standard deviation of 10^{-5} rad. This can be a reasonable value for real cameras. In particular, according to Barron et al. (1994) the correct value of noise introduced by the optical sensors can be quantified in 1 pixel. This value is also used in other works, such as Soatto et al. (1996) and Soatto and Perona (1997). However, this pixel information has to be translated into some meaningful quantity. We used the value of 10^{-5} rad, as in the paper by Segal and Gurfil to be as consistent as possible with their work. This is necessary to compare the obtained results. No justification is given in the aforementioned reference on that value. An information about the relationship between pixel and radians is given by the angular resolution. This quantity depends on the camera setup. It is possible to assume to have a noise mean standard deviation of 1 pixel and therefore a pixel size of 10^{-5} rad. This fits some cameras specification already adopted on past missions (Keller et al., 2009). **Q**, the process covariance matrix, has to be selected to ensure the convergence of the filter. Finally, the initial value of **P**, the error covariance matrix, represents the uncertainties in the initial estimation of the state. For each time step, the quaternion is normalized. According to the IEKF formulation, after the initial condition initialization, the predicted value of the state has to be computed using the dynamical model. The function *ode45* is used in MATLAB to integrate the set of dynamical equations, for the state, for each time step. Then, a centered difference method is used to compute the Jacobian of the process model. With this value, the transition matrix is computed and the new error covariance is predicted. At this point, a *while* cycle is used to implement the iterative procedure of the Iterated Extended Kalman Filter. A tolerance equal to 0.01 and a maximum number of iterations equal to 10 is used. The threshold indicates the percentage variation of the state vector norm with respect to the previous step. For the observation model, the equations are solved and linearized with the same approximate method. Finally, the filter innovation, innovation covariance and gain are iteratively computed and state and covariance are updated. Note that the quaternions are additively updated, imposing a normalization constraint. In our simulations, a time step of 1 s is used and the total time of the simulation is 100 s. The computed errors are defined as:

$$e_\rho = \sqrt{(\rho_x - \underline{\rho}_x)^2 + (\rho_y - \underline{\rho}_y)^2 + (\rho_z - \underline{\rho}_z)^2} \tag{49}$$

with e_ρ being the error of the estimation of the center of mass. In this notation, $\underline{\rho}$ denotes the estimated value of ρ. In the same way the relative translational velocity error can be defined:

$$e_{\dot{\rho}} = \sqrt{(\dot{\rho}_x - \underline{\dot{\rho}}_x)^2 + (\dot{\rho}_y - \underline{\dot{\rho}}_y)^2 + (\dot{\rho}_z - \underline{\dot{\rho}}_z)^2} \tag{50}$$

And the relative angular velocity error:

$$e_\omega = \sqrt{(\omega_x - \underline{\omega}_x)^2 + (\omega_y - \underline{\omega}_y)^2 + (\omega_z - \underline{\omega}_z)^2} \tag{51}$$

For k_1 and k_2 the error is simply:

$$e_{k_1} = \sqrt{(k_1 - \underline{k}_1)^2} \quad e_{k_2} = \sqrt{(k_2 - \underline{k}_2)^2} \tag{52}$$

The attitude error is defined in a different way. Recalling the definition of the inverse of a quaternion:

$$\mathbf{q}^{-1} = \frac{\mathbf{q}^*}{||\mathbf{q}||^2} \tag{53}$$

where $\mathbf{q}^*$ is the conjugate of $\mathbf{q}$, the error quaternion is equal to:

$$\mathbf{q}_e = \mathbf{q} \otimes \underline{\mathbf{q}}^{-1} \tag{54}$$

The symbol $\otimes$ is defined as the product of two quaternions. Finally, the attitude estimation error can be defined as in Markley and Mortari (2000):

$$e_\theta = 2\cos^{-1}(q_{e_0}) \tag{55}$$

where in our notation, q_{e_0} is the scalar part of the error quaternion. In the following examples, the performance of the filter is analyzed.

6.1. Case A – with pseudo-measurement constraint

For this simulation, the Eq. (37) is applied in the observation model as pseudo-measurement constraint. In the first case scenario, the filter is tested with the following initial conditions:

- $\boldsymbol{\rho}_0 = [10, 60, 10]$ m,
- $\dot{\boldsymbol{\rho}}_0 = [0.01, -0.0225, -0.01]$ m/s,
- $\boldsymbol{\omega}_0 = [-0.1, -0.1, 0.034]$ deg/s,
- $\mathbf{q}_0 = [0, 0, 0, 1]$.

The components of the covariance matrix are chosen to represent a realistic situation. In fact, for a space debris capture mission, it is realistic to assume to have partial information about the target position, velocity and attitude. Again, the values of the initial covariance recall the ones used in Segal et al. (2014). In particular, $\mathbf{P}$ is a diagonal matrix composed by:

- $\sigma_\rho^2 = [1, 1, 1]$ m^2;
- $\sigma_{\dot\rho}^2 = [1, 1, 1]$ m^2/s^2;
- $\sigma_\omega^2 = [1, 1, 1]$ deg^2/s^2;
- $\sigma_q^2 = [1, 1, 1, 1] \cdot 10^{-5}$;
- $\sigma_P^2 = [1, 1, 1]$ m^2;
- $\sigma_I^2 = [1, 1]$.

For this case, 100 simulations are considered. The mean relative errors after 10 s are evaluated according to Eqs. (49)–(52) and (55). The results are analyzed using histograms Figs. 11–16. In this work, both EKF and IEKF are used. However, only the results corresponding to the IEKF are here reported. The IEKF can present, in some applications, a less robust behavior with respect to its non-iterative form. In this case, the two methods were almost equal in terms of robustness. This is the main reason why results referred to the EKF are not presented. Please note that this work does not want to offer a complete and satisfactory analysis on the compared performance of the two filters. For sake of simplicity, simulations referring only to the best-performing method are discussed. Additional work and research has to be carried out to state a conclusive analysis of robustness assessment of the presented filters in different operational conditions. In particular, how different factors, such as the target dynamics, could affect the overall robustness of the filtering procedure have to be further analyzed.

The presented results show robust convergence in all the analyzed simulations. Fig. 5 displays how the position error quickly converges, also in the case of a large initial error. Consistently with the work by Segal, the steady state error of the relative position of the center of mass remains significant (0.5 m). This happens even if a low value for the noise associated to the optical measurements is adopted. Very good results are obtained for the relative angular and translational velocity in Figs. 6 and 7. This is probably connected to the fact that the optical flow equation is exploited. For the relative attitude, Fig. 8 shows poor convergence of the relative angle error. The error tends to remain close to the initial value. The two inertia ratios have good convergence thanks to the imposed equality constraint, as reported in Figs. 9 and 10. In Table 1, the results for are summarized. Table 1 shows the mean errors around its steady state value. This first case is comparable to the Segal's simulation (Segal et al., 2014). Despite the different method to compute the inertia properties, the initial conditions and the filtering procedure are similar. The error of the relative position, translational velocity and attitude is comparable to the one obtained to Segal. However, in this work, better performance are obtained in terms of relative angular velocity. Moreover, the inertia ratios are estimated with the same filtering procedure, allowing for an online implementation. As already said, this was not possible in the Segal's work.

6.1.1. Noise analysis

It can be expected that the noise level associated to the measurements influences the filtering procedure. An analysis, increasing the value of the measurements noise, has been carried out. The performance of the filter are analyzed using, as noise level, the values of 5e−5 and 1e−4 rad. Even if the global convergence of the filter is guaranteed, the

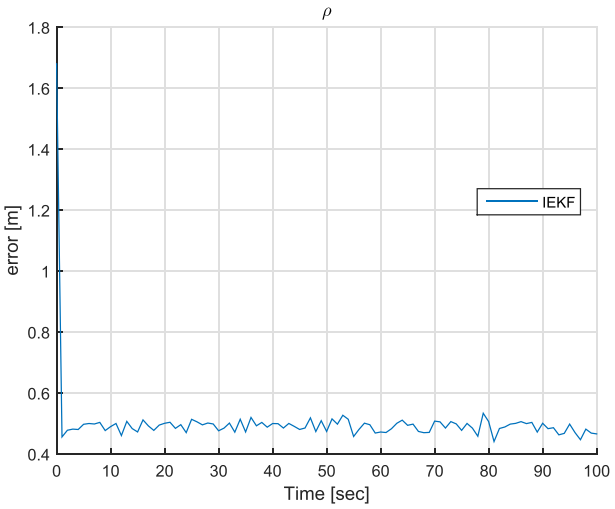

Fig. 5. Relative position error- Case A.

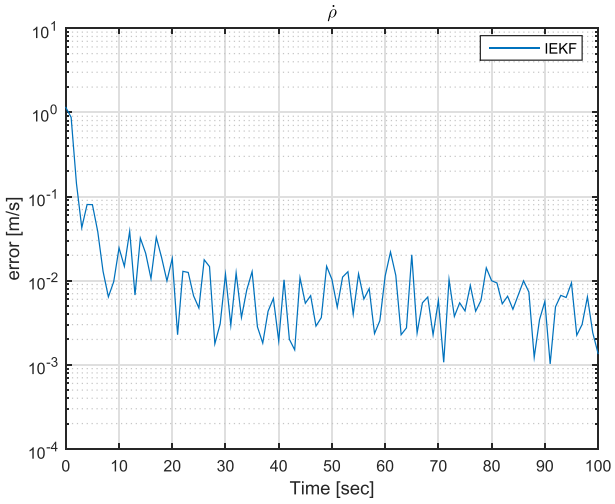

Fig. 6. Relative translational velocity error – Case A.

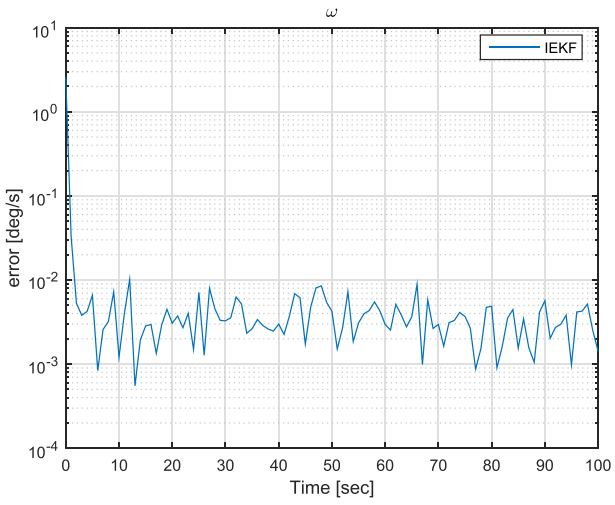

Fig. 7. Relative angular velocity error – Case A.

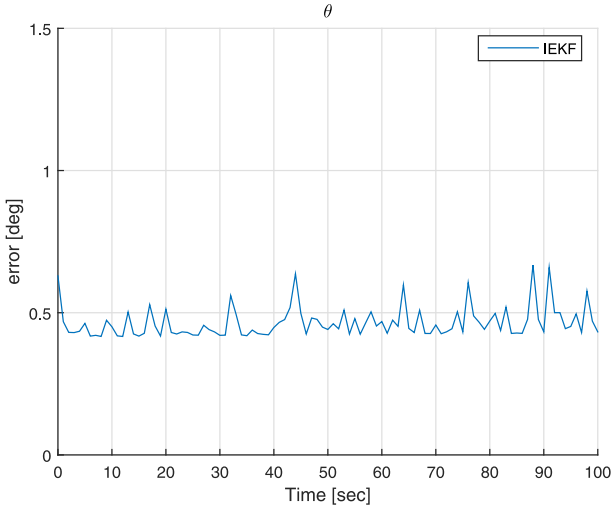

Fig. 8. Relative attitude error – Case A.

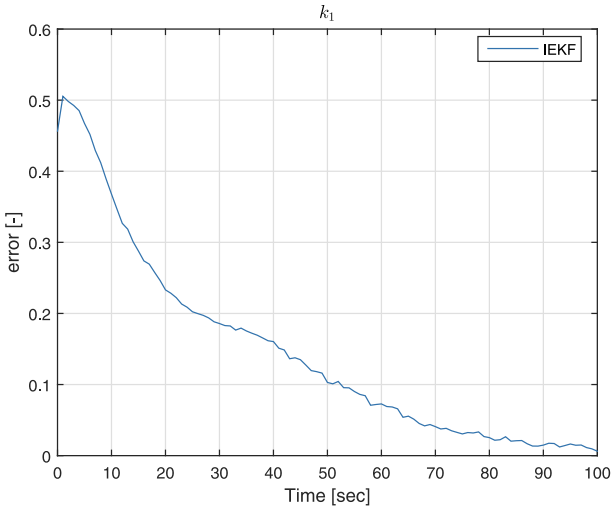

Fig. 9. k_1 Inertia ratio error – Case A.

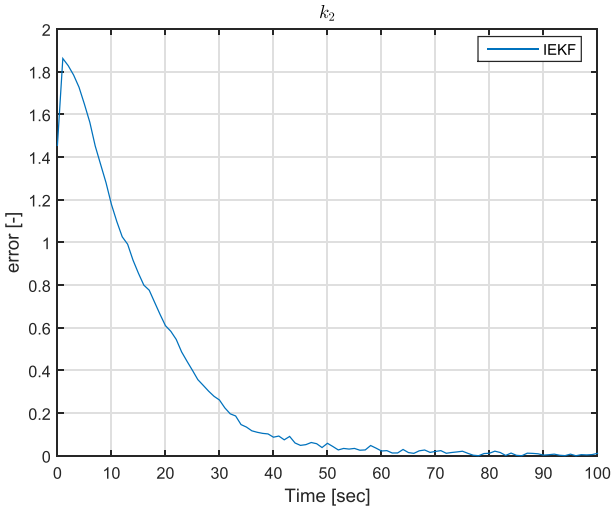

Fig. 10. k_2 Inertia ratio error – Case A.

Table 1
State errors – Case A.

Percentiles	ρ [m]	$\dot{\rho}$ [m/s]	ω [deg/s]	θ [deg]	k_1 [–]	k_2 [–]
50	0.51	0.0062	0.0035	0.49	0.067	0.037
70	0.64	0.0067	0.0036	0.61	0.13	0.051
90	0.73	0.0073	0.0039	0.77	0.24	0.23
100	0.90	0.011	0.0043	0.87	0.53	0.23

trend of the error start assuming an oscillating behavior. This can be partially limited by properly tuning the filter parameters. In the following Table 2, the mean steady state error for a single run for all the three different levels of noise is reported.

Despite an increase of the estimation errors for the relative position and velocity, the filtering procedure appears robust. However, an accurate tuning has to be performed to avoid large fluctuations.

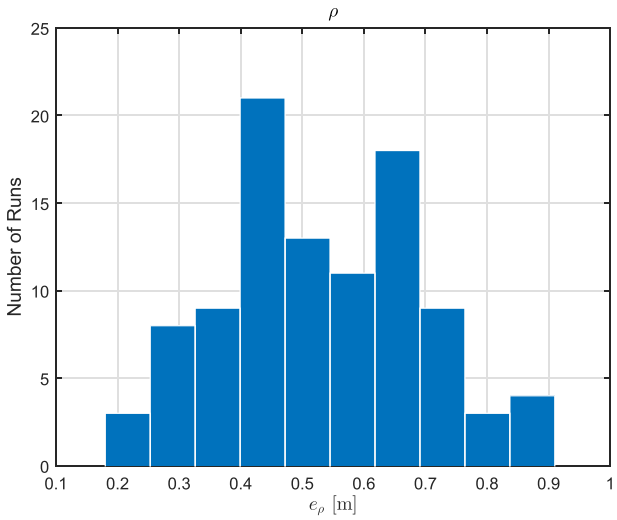

Fig. 11. Relative position error histogram – Case A.

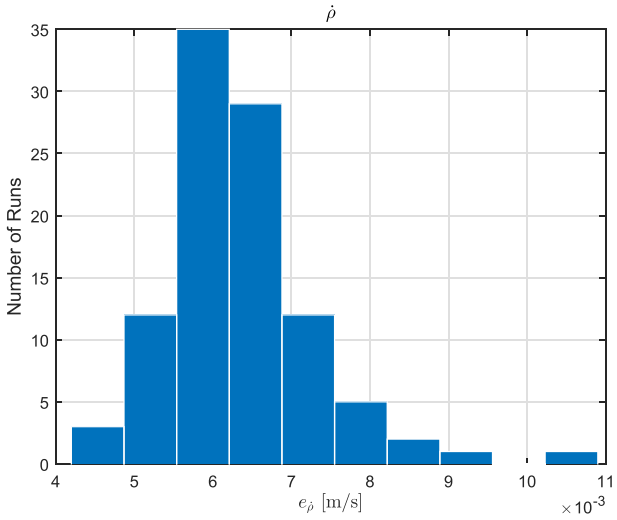

Fig. 12. Relative translational velocity error histogram – Case A.

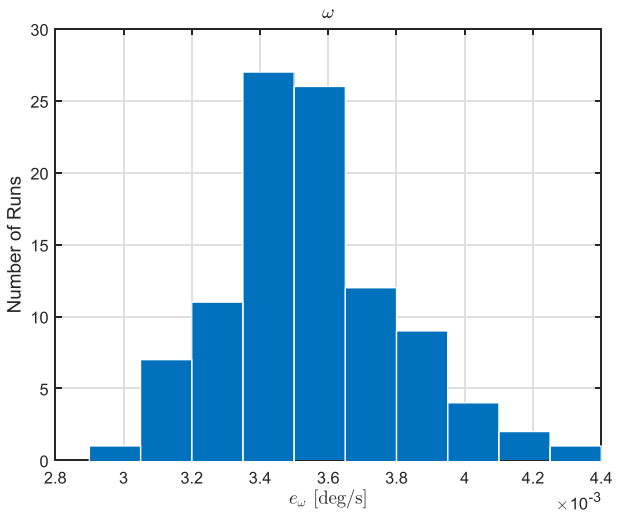

Fig. 13. Relative angular velocity error histogram – Case A.

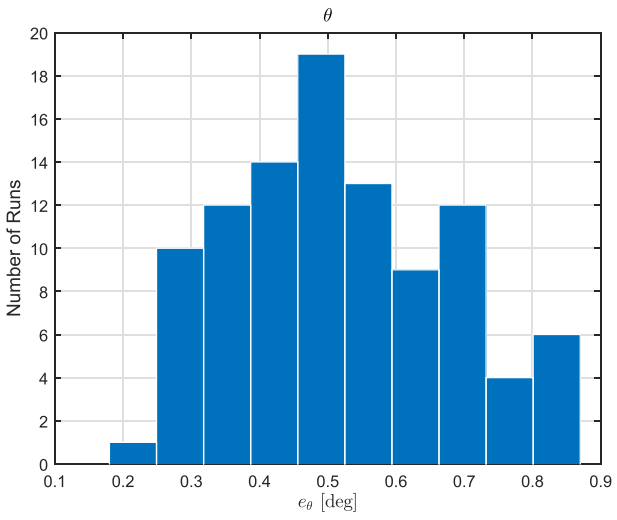

Fig. 14. Relative attitude error histogram – Case A.

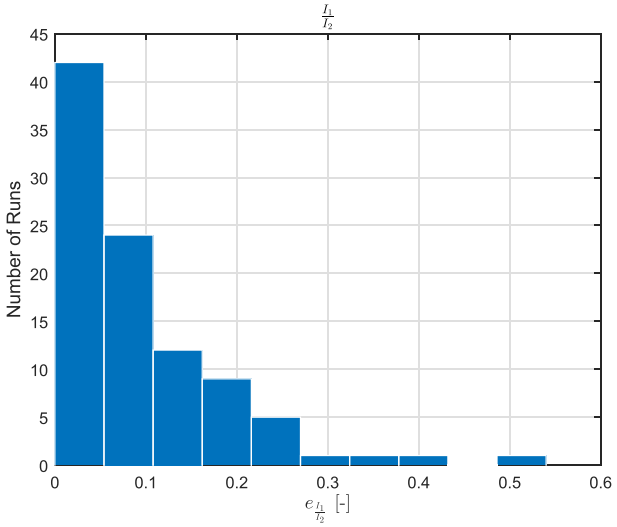

Fig. 15. k_1 Inertia ratio error histogram – Case A.

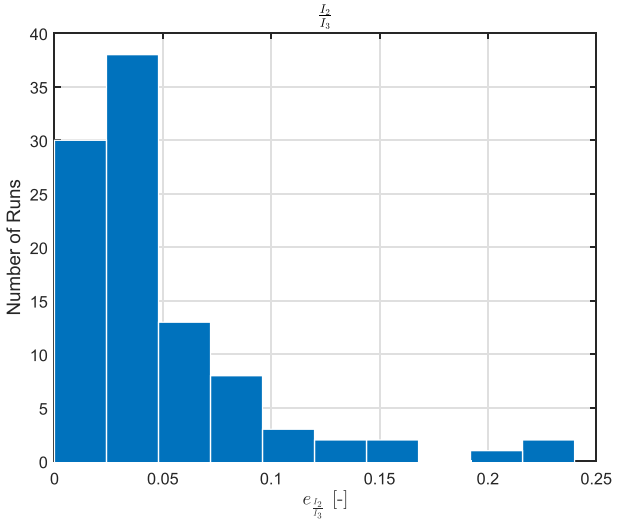

Fig. 16. k_2 Inertia ratio error histogram – Case A.

Table 2
State errors – different noise levels.

Noise Level	ρ [m]	$\dot{\rho}$ [m/s]	ω [deg/s]	θ [deg]	k_1 [–]	k_2 [–]
1e−5	0.26	0.010	0.0018	0.59	0.037	0.009
5e−5	0.35	0.02	0.003	0.63	0.04	0.01
1e−4	0.49	0.032	0.0041	0.67	0.06	0.01

6.2. Case B – without pseudo-measurement constraint

In this case, the equality constraint is removed. The Case A initial conditions are applied. For the covariance matrix, a smaller value is assumed for the inertia ratios:

- $\sigma_\rho^2 = [1,1,1]\ \mathrm{m}^2$,
- $\sigma_{\dot\rho}^2 = [1,1,1]\ \mathrm{m}^2/\mathrm{s}^2$,
- $\sigma_\omega^2 = [1,1,1]\ \mathrm{deg}^2/\mathrm{s}^2$,
- $\sigma_q^2 = [1,1,1,1]\cdot 10^{-5}$,
- $\sigma_P^2 = [1,1,1]\ \mathrm{m}^2$,
- $\sigma_I^2 = [1,1]/2$.

The filter keeps being robust under these new conditions too, and converges in most of the simulations. The position and translational velocity error trends do not change. In fact, the rotational dynamics does not affect the translation. The angular velocity and attitude errors trends are comparable to the Case A outputs. The small values for the angular velocity are the reason for these similarities. From the presented results, the inertia ratios errors seem to converge to zero. However, this is only due to the fact that the initial covariance is small. In fact, looking at the trend of the error in Figs. 17 and 18, it is clear how the error tends to be constant. This means that the estimated inertia ratios remain constant and do not converge. In Table 3, the error results are summarized.

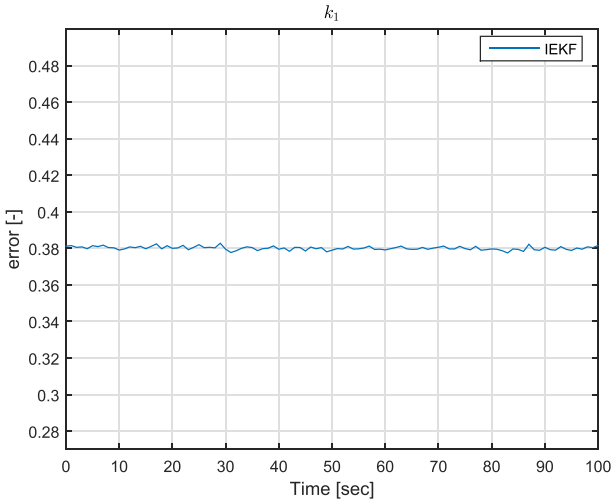

Fig. 17. k_1 Inertia ratio error – Case B.

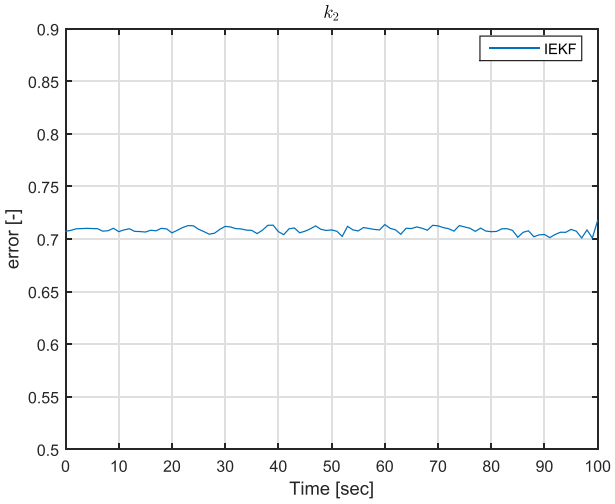

Fig. 18. k_2 Inertia ratio error – Case B.

Table 3
State errors – Case B.

Percentiles	ρ [m]	$\dot{\rho}$ [m/s]	ω [deg/s]	θ [deg]	k_1 [–]	k_2 [–]
50	0.51	0.0081	0.0058	0.59	0.33	0.35
70	0.6	0.009	0.0059	0.74	0.6	0.55
90	0.77	0.011	0.0063	0.88	1.4	1.6
100	0.96	0.013	0.0069	1.2	3.2	2.6

6.3. Case C – without constraint, high angular velocity

So far, only small values for the relative angular velocity have been considered. In this simulation, the performance of the filter without equality constraint is evaluated in a case with larger initial relative angular velocity. In particular:

- $\boldsymbol{\rho}_0 = [10, 60, 10]$ m,
- $\dot{\boldsymbol{\rho}}_0 = [0.01, -0.0225, -0.01]$ m/s,
- $\boldsymbol{\omega}_0 = [-1, -1, 0.934]$ deg/s,
- $\mathbf{q}_0 = [0, 0, 0, 1]$.

The value of $\boldsymbol{\omega}_0$ is obtained increasing the value of $\boldsymbol{\omega}_T$. The covariance matrix is, as before:

- $\sigma_\rho^2 = [1,1,1]\ \mathrm{m}^2$,
- $\sigma_{\dot\rho}^2 = [1,1,1]\ \mathrm{m}^2/\mathrm{s}^2$,
- $\sigma_\omega^2 = [1,1,1]\ \mathrm{deg}^2/\mathrm{s}^2$,
- $\sigma_q^2 = [1,1,1,1]\cdot 10^{-5}$,
- $\sigma_P^2 = [1,1,1]\ \mathrm{m}^2$,
- $\sigma_I^2 = [1,1]/2$.

Table 4 shows how the estimation of the relative position and translational velocities is slightly affected by the change in the angular velocity. The relative angular velocity and primarily the relative attitude are badly affected by this change. In fact, in this case, the error in the estimation of the inertia matrix strongly affects the dynamical model

Table 4
State errors – Case C.

Percentiles	ρ [m]	$\dot{\rho}$ [m/s]	ω [deg/s]	θ [deg]	k_1 [–]	k_2 [–]
50	0.53	0.01	0.012	1.8	0.035	0.021
70	0.64	0.013	0.013	2	0.043	0.024
90	0.76	0.017	0.014	2.2	0.069	0.032
100	0.94	0.02	0.016	2.5	0.15	0.043

propagation. Therefore, the incorrect inertia ratios lead to a decay in the estimation performance for angular velocity and attitude. However, using a larger value for the target angular velocity implies better results in the inertia ratios estimation also without the equality constraint imposed with the pseudo measurement and therefore, without exploiting any numerical derivation. Figs. 19 and 20 show the converging trend of the inertia ratios. This is justified by the fact that, with a larger angular velocity, the filtering process better performs in the estimation of the inertia components. Hence, the dynamical model and the measurement equations of the angular velocity, force the inertia ratios to converge to a 'consistent' and exact value. This estimation can be obtained, in torque free motion conditions, only parameterizing the inertia matrix in a proper way, without using any numerical derivation.

7. Inertia reconstruction

In the previous section, the estimation process of the inertia ratios has been shown. However, the inertia parameters, with small relative angular velocity, are correctly recovered only if information about the angular acceleration of the target is provided. This implies to numerically derive the available measures of the angular velocity. Numerical derivatives of a quantity that is usually noisy, can introduce instabilities and produce inaccurate results. Moreover, only the inertia ratios are obtained. With these quantities, no information about the actual mass distribution can be retrieved. In this section, a method to recover

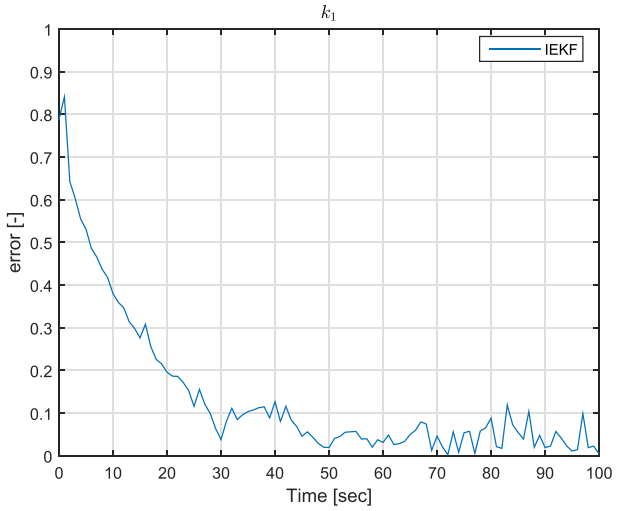

Fig. 19. k_1 Inertia ratio error – Case C.

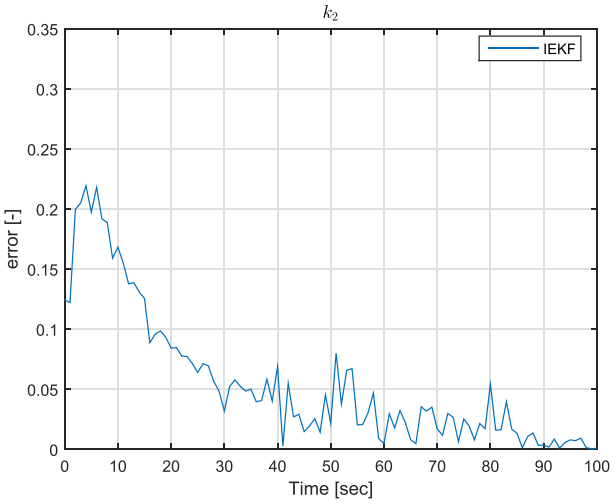

Fig. 20. k_2 Inertia ratio error- Case C.

all the inertia components is described, without relying on any numerical method. A video and image process to recover mass properties is presented. This method is not computationally efficient and, in our application, relies on free and not optimized video/image processing software. The main idea is to collect a video or images of the observed body. From this set of images, a point cloud can be constructed according to video processing algorithms. Once a point cloud is available, a triangulate mesh can be built. The mesh gives us information about the geometry of the object. At this point, an assumption has to be done. In fact, knowing the geometry, the unknown density properties of the object do not allow a complete reconstruction of the mass properties of the body. However, generalizing the problem, the density can be assumed constant. In our case, for sake of simplicity, a value of 1 $\frac{g}{cm^3}$ is used. This value can be easily modified, according to the application. This is a strong assumption and can be acceptable only in very few cases. This procedure has been experimentally validate at the University of Florida to demonstrate the validity of this method also with complex geometries. A very simple experimental setup is used. The video of a 3-DOF simulator (Fig. 21) are collected using a Sony HandyCam HDR-CX110. The obtained images are imported with VisualSFM (Wu, 2011) and the point cloud is extracted. Then, with MeshLab (Cignoni et al., 2008) a mesh is created. This mesh is exported to MATLAB (Fig. 22) and the mass properties are recovered. The computer used for the video processing mounts an Intel Xeon E5-2609 2.5 Ghz 10 Mb cache Ivy Bridge Processor, 16 Gb DDR3 SDRAM and a PNY Quadro K620 2 Gb Video Card. The obtained results show how the volume of the object can be reconstructed with this procedure. In particular, the resulting errors of the component of the inertia matrix are always lower than 20% with respect to the reference value. This is obtained using a CAD model of the 3-DOF simulator, imposing the same constant density.

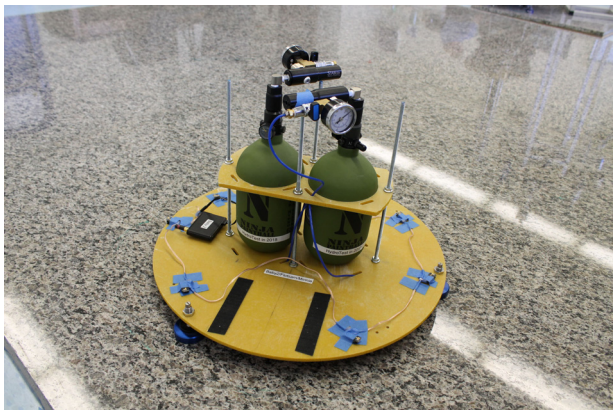

Fig. 21. 3-DOF simulator.

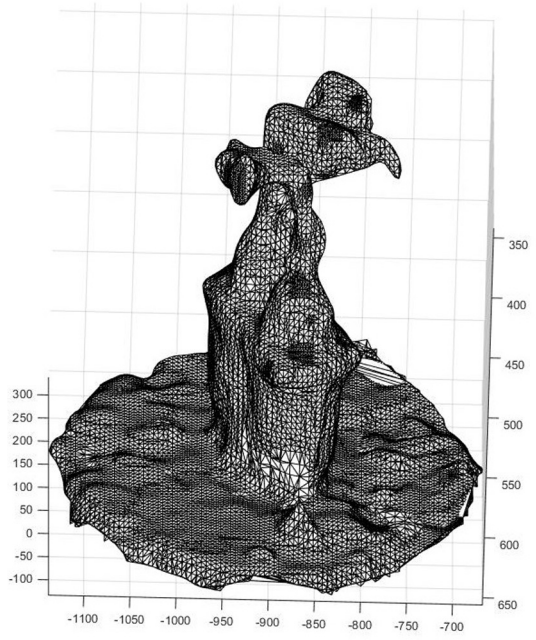

Fig. 22. MATLAB mesh.

8. Conclusion

This work proposes a new algorithm for estimating the pose, motion and inertia properties of an unknown, uncooperative space object. The presented results show how the algorithm, exploiting the equality constraint, allows for a precise estimation of the complete relative state and the inertia components. Moreover a quick convergence and a satisfactory accuracy are guaranteed. Several simulations are presented to demonstrate the robustness of the algorithm with different covariance matrix values and initial conditions. Moreover, it has been shown how the inertia components, in the filtering process, can converge without the equality constraint but only with a sufficiently high value for the target angular velocity. In most of the cases, the presented algorithm shows better results with respect to similar works. A novel approach to estimate the inertia components with very limited computational burden is proposed. It is important to underline that the presented validation does not include any stereovision algorithm. This a crucial aspect for both computational efficiency and filter convergence. A proper feature extraction and matching method has to be used and a proper method for the tracking has to be selected. These methods must be computationally light but also very robust. In fact, during a close approach with a completely unknown object, it is possible to face very different lighting and reflectance conditions. Moreover, occlusions and self-occlusions can often occur. In all these cases, the computer vision algorithm must assure a good and precise information about the feature points on the object. Especially in case of occlusions, the number of features has to be high enough to ensure robustness. Moreover, the low measurement noise level used in this work has to be guaranteed by a proper setup and a robust computer vision algorithm. For this reason, the proposed estimation procedure could not be the best choice for missions with low cost hardware or without a very good computer vision architecture. In addition, it has been shown how the inertia properties can be reconstructed with a video processing procedure. In fact, the geometrical properties of a body can be reconstructed collecting multiple frames in time; the mass properties of the observed object can be then reconstructed under a uniform density distribution assumption. The step further in the research asks for the experimental campaign to validate the promising obtained numerical results and to tune the algorithms.

References

Barron, J.L., Fleet, D.J., Beauchemin, S.S., 1994. Performance of optical flow techniques. Int. J. Comput. Vision 12, 43–77.

Benninghoff, H., Boge, T., 2015. Rendezvous involving a non-cooperative, tumbling target – estimation of moments of inertia and center of mass of an unknown target. In: International Symposium on Space Flight Dynamics.

Biesbroek, R., Soares, T., Husing, J., Innocenti, L., 2013. The e. deorbit cdf study: a design study for the safe removal of a large space debris. In: ESA Special Publication, p. 79.

Bryson, M., Sukkarieh, S., 2007. Building a robust implementation of bearing-only inertial slam for a UAV. J. Field Robot. 24, 113–143.

Cignoni, P., Callieri, M., Corsini, M., Dellepiane, M., Ganovelli, F., Ranzuglia, G., 2008. Meshlab: an open-source mesh processing tool. In: Eurographics Italian Chapter Conference. The Eurographics Association, pp. 129–136.

Clohessy, W.H., Wiltshire, R.S., 1960. Terminal guidance system for satellite rendezvous. J. Aerosp. Sci. 27 (9), 653–658.

Croomes, S., 2006. Overview of the dart mishap investigation results. NASA Rep., 1–10

DAmico, S., Benn, M., Jørgensen, J.L., 2014. Pose estimation of an uncooperative spacecraft from actual space imagery. Int. J. Space Sci. Eng. 2, 171–189.

Dong, G., Zhu, Z., 2016a. Incremental inverse kinematics based vision servo for autonomous robotic capture of non-cooperative space debris. Adv. Space Res. 57, 1508–1514.

Dong, G., Zhu, Z.H., 2016b. Autonomous robotic capture of non-cooperative target by adaptive extended kalman filter based visual servo. Acta Astronaut. 122, 209–218.

Felicetti, L., Sabatini, M., Pisculli, A., Gasbarri, P., Palmerini, G.B., 2014. Adaptive thrust vector control during on-orbit servicing. In: Proceedings of AIAA SPACE 2014 Conference and Exposition, paper AIAA-2014-4341, San Diego.

Fenton, R.C., 2008. A LADAR-Based Pose Estimation Algorithm for Determining Relative Motion of a Spacecraft for Autonomous Rendezvous and Dock. ProQuest.

Friend, R.B., 2008. Orbital express program summary and mission overview. In: SPIE Defense and Security Symposium, International Society for Optics and Photonics, p. 695803.

Galvez, A., Carnelli, I., Michel, P., Cheng, A., Reed, C., Ulamec, S., Biele, J., Zbrll, P., Landis, R., 2013. Aida: The asteroid impact & deflection assessment mission. In: European Planetary Science Congress, EPSC2013-1043.

Grasa, O.G., Civera, J., Montiel, J., 2011. Ekf monocular slam with relocalization for laparoscopic sequences. In: 2011 IEEE International Conference on Robotics and Automation (ICRA). IEEE, pp. 4816–4821.

Gurfil, P., Kholshevnikov, K.V., 2006. Manifolds and metrics in the relative spacecraft motion problem. J. Guid. Control Dynam. 29, 1004–1010.

Heeger, D.J., Jepson, A.D., 1992. Subspace methods for recovering rigid motion I: algorithm and implementation. Int. J. Comput. Vision 7, 95–117.

Kaess, M., Ranganathan, A., Dellaert, F., 2007. isam: Fast incremental smoothing and mapping with efficient data association. In: 2007 IEEE International Conference on Robotics and Automation. IEEE, pp. 1670–1677.

Kaess, M., Ranganathan, A., Dellaert, F., 2008. isam: Incremental smoothing and mapping. IEEE Trans. Robot. 24, 1365–1378.

Kalman, R.E., 1960. A new approach to linear filtering and prediction problems. J. Fluids Eng. 82, 35–45.

Keller, H., Barbieri, C., Lamy, P., Rickman, H., Rodrigo, R., Wenzel, K. P., Sierks, H., A'Hearn, M., Angrilli, F., Angulo, M., et al., 2009. 4-osiris: The scientific camera system onboard rosetta. In: ROSETTA ESA's Mission to the Origin of the Solar System. Springer Science+ Business Media, pp. 315–382.

Kimball, P., 2011. Iceberg-relative navigation for autonomous underwater vehicles (Ph.D.). Stanford University, Stanford, CA, 8, 2011.

Lichter, M.D., Dubowsky, S., 2004. State, shape, and parameter estimation of space objects from range images. In: 2004 IEEE International Conference on Robotics and Automation, 2004. Proceedings. ICRA'04. IEEE, pp. 2974–2979.

Lichter, M.D., Dubowsky, S., 2005. Shape, motion, and parameter estimation of large flexible space structures using range images. In: Proceedings of the 2005 IEEE International Conference on Robotics and Automation, 2005. ICRA 2005. IEEE, pp. 4476–4481.

Listmann, K.D., Zhao, Z., 2013. A comparison of methods for higher-order numerical differentiation. In: 2013 European Control Conference (ECC). IEEE, pp. 3676–3681.

Liu, L., Zhao, G., Bo, Y., 2016. Point cloud based relative pose estimation of a satellite in close range. Sensors 16, 824.

Markley, F.L., Mortari, D., 2000. Quaternion attitude estimation using vector observations. J. Astronaut. Sci. 48, 359–380.

Maybeck, P.S., 1982. Stochastic Models, Estimation, and Control, vol. 3. Academic press.

McGee, L.A., Schmidt, S.F., 1985. Discovery of the kalman filter as a practical tool for aerospace and industry.

Opromolla, R., Fasano, G., Rufino, G., Grassi, M., 2015a. A model-based 3d template matching technique for pose acquisition of an uncooperative space object. Sensors 15, 6360–6382.

Opromolla, R., Fasano, G., Rufino, G., Grassi, M., 2015b. Uncooperative pose estimation with a lidar-based system. Acta Astronaut. 110, 287–297.

Philip, N., Ananthasayanam, M., 2003. Relative position and attitude estimation and control schemes for the final phase of an autonomous docking mission of spacecraft. Acta Astronaut. 52, 511–522.

Qian, N., 1997. Binocular disparity and the perception of depth. Neuron 18, 359–368.

Segal, S., Carmi, A., Gurfil, P., 2011. Vision-based relative state estimation of non-cooperative spacecraft under modeling uncertainty. In: 2011 IEEE Aerospace Conference. IEEE, pp. 1–8.

Segal, S., Carmi, A., Gurfil, P., 2014. Stereovision-based estimation of relative dynamics between noncooperative satellites: Theory and experiments. IEEE Trans. Control Syst. Technol. 22, 568–584.

Segal, S., Gurfil, P., 2009. Effect of kinematic rotation-translation coupling on relative spacecraft translational dynamics. J. Guid. Control Dynam. 32, 1045–1050.

Shahid, K., Okouneva, G., 2007. Intelligent lidar scanning region selection for satellite pose estimation. Comput. Vision Image Underst. 107, 203–209.

Sharma, S. et al., 2016. Comparative assessment of techniques for initial pose estimation using monocular vision. Acta Astronaut. 123, 435–445.

Soatto, S., Frezza, R., Perona, P., 1996. Motion estimation via dynamic vision. IEEE Trans. Autom. Control 41, 393–413.

Soatto, S., Perona, P., 1997. Recursive 3-d visual motion estimation using subspace constraints. Int. J. Comput. Vision 22, 235–259.

Strasdat, H., Montiel, J., Davison, A.J., 2010. Real-time monocular slam: Why filter? In: 2010 IEEE International Conference on Robotics and Automation (ICRA). IEEE, pp. 2657–2664.

Tweddle, B.E., 2013. Computer vision-based localization and mapping of an unknown, uncooperative and spinning target for spacecraft proximity operations (Ph.D.). Massachusetts Institute of Technology, Cambridge, MA.

Tweddle, B.E., Saenz-Otero, A., 2014. Relative computer vision-based navigation for small inspection spacecraft. J. Guid. Control Dynam., 1–9

Wu, C., 2011. Visualsfm: A visual structure from motion system. <http://homes. cs. washington. edu/∼ ccwu/vsfm 9>